A Truncated Manganese Spinel Cathode for Excellent Power and Lifetime in Lithium-Ion Batteries

6 AUTHORS, INCLUDING:

Joo-Seong Kim
Korea Advanced Institute of Science and Tech…
19 PUBLICATIONS   288 CITATIONS

SEE PROFILE

Jang Wook Choi
Korea Advanced Institute of Science and Tech…
115 PUBLICATIONS   6,406 CITATIONS

SEE PROFILE

A Truncated Manganese Spinel Cathode for Excellent Power and Lifetime in Lithium-Ion Batteries

Joo-Seong Kim,[†] KyungSu Kim,[‡] Woosuk Cho,[§] Weon Ho Shin,[†] Ryoji Kanno,*[,‡] and Jang Wook Choi*[,†]

[†]Graduate School of EEWS (WCU) and KAIST Institute NanoCentury, Korea Advanced Institute of Science and Technology (KAIST), 291 Daehak-ro, Yuseong-gu, Daejeon 305-701, Republic of Korea

[‡]Department of Electronic Chemistry, Interdisciplinary Graduate School of Science and Engineering, Tokyo Institute of Technology, 4259 Nagatsuta, Midori-ku, Yokohama 226-8502

[§]Advanced Batteries Research Center, Korea Electronics Technology Institute (KETI), Bundang-gu, Seongnam-si, Gyeonggi-do 463-816, Korea

S *Supporting Information*

ABSTRACT: Spinel-structured lithium manganese oxide ($LiMn_2O_4$) cathodes have been successfully commercialized for various lithium battery applications and are among the strongest candidates for emerging large-scale applications. Despite its various advantages including high power capability, however, $LiMn_2O_4$ chronically suffers from limited cycle life, originating from well-known Mn dissolution. An ironical feature with the Mn dissolution is that the surface orientations supporting Li diffusion and thus the power performance are especially vulnerable to the Mn dissolution, making both high power and long lifetime very difficult to achieve simultaneously. In this investigation, we address this contradictory issue of $LiMn_2O_4$ by developing a truncated octahedral structure in which most surfaces are aligned to the crystalline orientations with minimal Mn dissolution, while a small portion of the structure is truncated along the orientations to support Li diffusion and thus facilitate high discharge rate capabilities. When compared to control structures with much smaller dimensions, the truncated octahedral structure as large as 500 nm exhibits better performance in both discharge rate performance and cycle life, thus resolving the previously conflicting aspects of $LiMn_2O_4$.

KEYWORDS: *Lithium ion battery, cathode material, manganese spinel, truncation, manganese dissolution, cycle life*
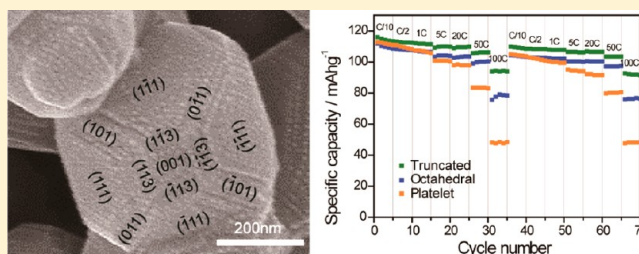
As the territory of lithium ion batteries (LIBs) is expanding toward large-scale applications,[1,2] such as hybrid electrical vehicles and utility power grids, the required properties of electrode materials have become more demanding. The active materials should be produced from raw materials that are cheap, abundant, and scalable. Also, the electrodes should provide good electrochemical performance with regard to energy/power density, lifetime, and safety. These challenging standards have driven the battery community to investigate diverse cathode materials based on a number of crystal frameworks (layered,[3] olivine,[4,5] triplite,[6] tavorite,[7,8] etc.) containing different transition metals. Although the community has made considerable progress in finding new promising structures, optimizing well-established materials[9] would be practically more preferable to meet the requirements of those emerging applications in a timely manner.

Among the existing cathode materials, lithium manganese oxide ($LiMn_2O_4$) with the spinel framework has been considered as one of the most viable cathodes for large-scale applications for a number of critical reasons: (1) Above all, its raw materials are cheap and abundant. (2) Its three-dimen-sional (3D) channel structure is highly desirable for efficient Li diffusion and thus for high rate operations. (3) Fundamental problems and properties have been identified and studied for years. (4) It holds safe characteristic and is also environmentally benign. (5) Finally, its operation potential (~4.1 V vs Li/Li$^+$) is almost the highest within stable potential windows of most electrolytes. Some high potential cathodes[10,11] operating at higher than 4.5 V were developed, but the unstable nature of most electrolytes in those potentials tends to hinder their robust cycling. Despite these advantageous properties,[12,13] however, $LiMn_2O_4$ has suffered from a limited cycle life originating from Mn dissolution,[14,15] which has been known to be associated with the well-known disproportionation[15−18] of Mn^{3+} generating soluble Mn^{2+}: $2Mn^{3+}_{(solid)} \rightarrow Mn^{4+}_{(solid)} + Mn^{2+}_{(solution)}$. Extensive studies have revealed that the dissolved Mn ions destabilize the electrode/electrolyte interfaces of both cathodes[17,19] and anodes,[18−20] thus impairing reversibility of

charging–discharging. Also, the characterization of simplified samples has indicated[17] that the Mn dissolution is largely dependent on the lattice orientation of the surface interfacing with electrolytes. An ironical feature with regard to the Mn dissolution is that the {110} surfaces whose orientations are aligned to Li diffusion channels are most vulnerable to Mn dissolution.[17,21,22] Thus, from the crystalline orientation viewpoint, the maximization of power performance could, in turn, deteriorate the cycle life. To date, none of the reported $LiMn_2O_4$ structures has resolved these two contradictory but critical aspects of $LiMn_2O_4$ within the given crystal structures. Most of the recent investigations demonstrating impressive power performance focused only on scaling-down the dimensions[12,13,21] of $LiMn_2O_4$ to decrease electronic and ionic diffusion pathways but overlooked the crystal orientation of $LiMn_2O_4$ that affects its cycle life significantly.

As an attempt to address the two incompatible aspects of $LiMn_2O_4$, herein, we develop a crystal structure, namely, a truncated octahedron, where most surfaces are aligned to the crystal orientations activating minimal Mn dissolution, while a small portion of surfaces are truncated along the directions that support Li diffusion and therefore its intrinsic power performance. As compared to control samples with even smaller dimensions, the truncated octahedral structure bearing the dual lattice orientations within a single crystal structure exhibits far better performance in both power and cycle life. Although various treatments such as surface coating,[18,23,24] Li-rich composition,[15] and doping with foreign elements[15,25,26] have been effective in improving the cycling performance by decreasing Mn dissolution, these treatments are often required to sacrifice capacity and/or power capability. In particular, the Li rich strategy has been frequently involved because it makes the Mn valence state away from +3 and therefore effectively suppresses the dissolution. In contrast, the truncation of the crystal structure described herein does not deteriorate these other important properties.

The truncated octahedral structure is schematically illustrated in Figure 1a, alongside other control structures including an
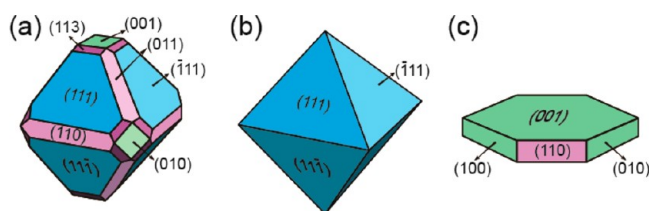

Figure 1. Schematic illustration of $LiMn_2O_4$ with various crystal shapes. (a) Truncated octahedron (Oh^T). (b) Bare octahedron (Oh). (c) platelet (PL). The surfaces with equivalent crystal orientations are presented in the same colors.

octahedral structure with no truncation (Figure 1b) and nanoplatelet (Figure 1c). Hereafter, we denote the truncated octahedron, bare octahedron, and platelet as Oh^T, Oh, and PL, respectively. As described in the Experimental Section, the syntheses of these structures were done by preparing manganese oxide or manganese hydroxide compounds with the corresponding morphologies, followed by solid state reactions with Li precursors. Thus, the morphology control at the stage of manganese oxide or manganese hydroxide is crucial and was indeed enabled by tuning key synthetic parameters including temperature, Mn precursor, and surfactant. While

$Mn(OH)_2$ PLs were synthesized following the established procedures developed for Ni counterparts,[27] the truncation of Oh was facilitated by minute temperature controls during the hydrothermal synthesis (Oh^T: 220 °C, Oh: 200 °C). Typically, truncated lattice planes bearing higher surface energies are more probable to be formed at higher temperatures[28] or after longer reaction times.[29] Among the {110}, {100}, and {111} surfaces, it has been known that the surface energy increases in the sequence of {111}, {100}, and {110}.[30] Thus, at a relatively higher temperature of 220 °C, the lattice surfaces with all of the three orientations are preferable to be formed, resulting in the formation of Oh^T. In contrast, at a lower temperature of 200 °C, only the lowest energy surfaces {111} are preferred, leading to the formation of Oh. It should be also noted that, in this study, the stoichiometric ratio between Li and Mn was fixed to 1.09:2 during the synthesis for all of the structures to pay our attention mainly to the morphology effect. Consistent stoichiometry over the samples was confirmed by inductively coupled plasma atomic emission spectrometry (ICP-AES) characterization, as the characterization indicates that the Li:Mn ratios are 0.550, 0.552, and 0.543 for Oh^T, Oh, and PL, respectively. The morphology of Mn_3O_4 or $Mn(OH)_2$ was characterized by scanning electron microscope (SEM) and transmission electron microscope (TEM), and it was confirmed that all of the morphologies are determined at this stage (Supporting Information, Figures S1 and S2).

X-ray diffraction (XRD) patterns for all of the three compounds are presented in Figure 2. All of those patterns can be perfectly assigned to the spinel framework of $LiMn_2O_4$ under the $Fd\bar{3}m$ space group, thus verifying that the synthesized compounds hold the proper crystallinity without impure phases. More importantly, the relative peak intensities reflect the dominant surface orientations of each compound. Between Oh^T and Oh, when all of the peaks are normalized by the peak assigned to the dominant (111) octahedral orientation, Oh^T exhibits more intensified peaks corresponding to the truncated surface orientations such as (400), (440), and (311). Similarly, the pattern of PL exhibits relatively higher peaks assigned to its surface plane of (400). For the case of PL, the peak intensities corresponding to some other orientations including (311) and (440) are also enhanced compared to those of Oh^T and Oh, which is due to relatively weakened normalization (111) peak.

The morphology and crystal structure of Oh^T were further characterized by SEM and TEM. As displayed in Figure 3a and b, typical dimensions of Oh^T are 400−600 nm. The SEM image in Figure 3b clearly visualizes the truncated surfaces at the vertices and edges of the parental octahedral structure, and the orientation of each surface was assigned following the established face orientation of the octahedral face-center cubic (fcc) framework, that is, {111},[28−30] as well as those of its truncated derivatives.[28−31] TEM characterizations conducted at various orientations also support the assigned truncated crystal structure. For the TEM observation at each orientation (see structural schematics in Figure 3c–e), a high-resolution (HR) TEM image (Figure 3f–h), the resultant Fast Fourier-transformed (FFT) pattern (insets of Figure 3f–h), and the zone axis were attained. When viewed along the direction normal to the truncated vertex surface (Figure 3c), an HRTEM image shows lattice fringes with a lattice distance of 2.06 Å along the {400} directions. The FFT pattern obtained from the HRTEM image exhibits spots that correspond to the lattice orientations as denoted in the inset. Also, the FFT pattern indicates the zone axis of the electron-beam is along the [001]
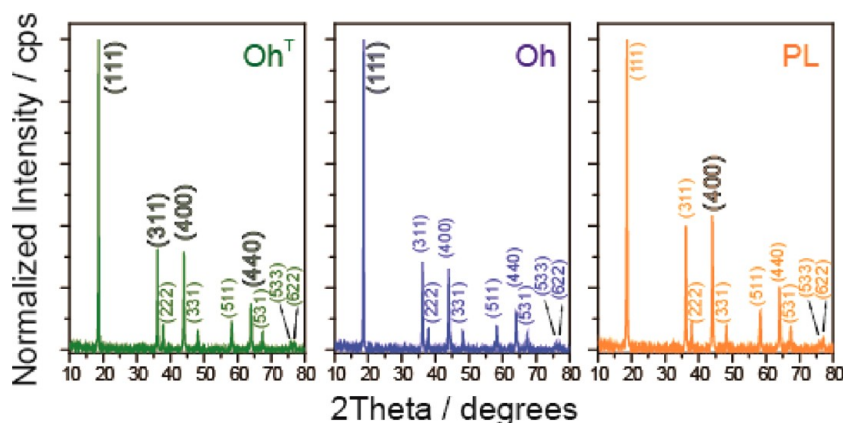
Figure 2. XRD patterns of LiMn$_2$O$_4$ with various crystal shapes. The lattice orientations corresponding to major peaks are denoted. All of the peaks in each sample were normalized by the (111) peak, and the peaks showing relatively higher intensities compared to those of other samples are denoted in bold.

direction, which is consistent with the orientation of the truncated surface. Similarly, when viewed along the directions normal to the truncated edge surface (Figure 3d) and the octahedral surface (Figure 3e), lattice fringes along the {111} and {220} directions were observed, respectively (Figure 3g and h). Also, the resultant zone axis is consistent with the orientation of each truncated surface.

The same characterization was performed for Oh and PL (Figure 4). While low-magnification SEM images (Figure 4a and b) confirm the designated morphologies of both structures, higher magnification SEM images (Figure 4c and d) give dimensional information: dimensions of 400−600 nm for Oh, and edge lengths around 100−200 nm and thicknesses around 40−60 nm for PL (Supporting Information, Figure S3). As in the case of Oh^T, HRTEM images as well as their FFT patterns and resultant zone axes of the electron-beam were obtained for Oh and PL (Figure 4e and f), and the series of data are consistent with the properties of each crystal structure.

Electrochemical properties of all of the three samples were analyzed by preparing coin-type half-cells in which Li metal serves as both the counter and reference electrodes. Detailed cell fabrication and measurement conditions were presented in the Experimental Section. Owing to the proper crystallinity of the spinel LiMn$_2$O$_4$ structure, all of the three samples show potential profiles that match well with those of the reported LiMn$_2$O$_4$.[1,12,13,15,17,20,21,24,26] As shown in Figure 5a, the profiles exhibit two plateaus at 4.15 and 4.05 V during the charge and 4.10 and 4.0 V during the discharge. The presence of the two plateaus has been known[32] to originate from two different reaction modes: Depending on Li content (x value in Li$_x$Mn$_2$O$_4$), the two-phase reaction (smaller x region) and one-phase reaction (larger x region) take place in separate voltage windows. The relatively flat voltage profiles in the higher voltage region and the relatively steeper voltage profiles in the lower voltage region are reflective of the two-phase and one-phase reaction modes, respectively.

It has been found[17,21] that the well-established 3D ionic channels endow LiMn$_2$O$_4$ with outstanding rate performance. Motivated by the impressive results reported previously,[12,13,21] we have also tested the rate performance for all of the three samples by employing different C-rates. As shown in Figure 5b, Oh^T exhibits excellent rate performance such that when the C-rate increases even a thousand-fold from 0.1 to 100C, the cell still retains 81.1% of the original capacity (116 mAh g^{-1}). This

retention is quite remarkable considering that 100C corresponds to ~30 s for discharge and its rate performance is even better than that of much thinner (~10 nm in diameter) nanowires reported previously.[13] By contrast, Oh and PL show inferior performance of only 70.0 and 43.8% capacity retention under the same conditions of the C-rate increase. The trend between the samples is preserved at other high C-rates and is indeed reflected by distinct overpotentials in Figure 5c. At each C-rate, the overpotential decreases in the sequence of Oh^T, Oh, and PL. The enhanced rate performance of Oh^T, against that of Oh, PL, and the reported nanowires, suggests that the surface orientation of the active compound is more critical for the rate performance than the dimensions. The much inferior performance of PL is noteworthy considering that its thickness is only ~50 nm (Supporting Information, Figure S3). Although PL contains {110} surfaces (Figure 1c), on the whole, the unstable interfacial character of other dominant faces (discussed below) has a detrimental effect on the rate performance. It is noted that even Oh shows a better rate performance compared to those of most practical electrodes, which must be mainly due to its smaller mass loadings and particle sizes. However, the current mass loadings (listed in the Experimental Section) are at a similar level to those in most scientific publications, and the distinctive performance among the given morphologies is still valid. Also, it should be addressed that the better rate performance of Oh^T compared to that of Oh should be mainly from truncation, as both samples hold similar dimensions of 400−600 nm according to SEM characterization of a large number of both samples ($N \sim 50$).

Once again, the Mn dissolution tends to form unstable solid electrolyte interphase (SEI) layers on the electrode surfaces[17] and is thus very critical for the cycle lives of LiMn$_2$O$_4$ cathodes. Also, it should be noted that the Mn dissolution is largely dependent on the crystalline orientation of the surface exposed to the electrolyte. As expected from our original design concept of Oh^T that the dominant {111} surfaces minimize the Mn dissolution, Oh^T exhibits a far superior cycle life compared to that of PL in which its dominant {100} surfaces suffer from severe Mn dissolution. When each cycle is charged at 1C and discharged at 10C at room temperature (Figure 6a), Oh^T preserves 90.8% of its initial capacity (111 mAh g^{-1}) after 400 cycles, whereas PL exhibits abrupt decays in its capacity around 200 cycles and retains only 56.8% of its initial capacity after the same 400 cycles. As expected from the same dominant {111}
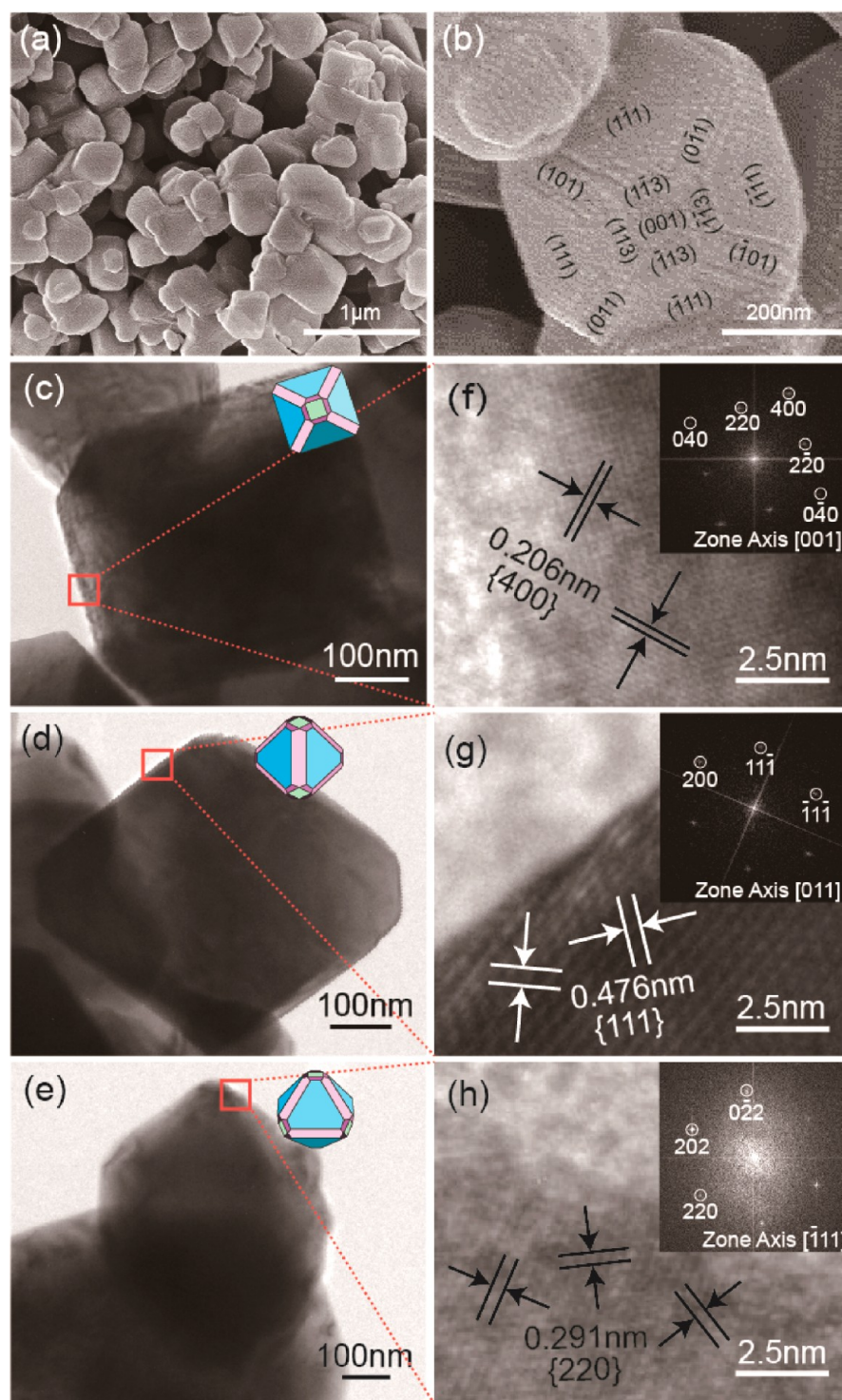
Figure 3. SEM and TEM characterizations of Oh^T. SEM images at (a) low and (b) high magnifications. (c−e) TEM images taken at different orientations as indicated by structural schematic in each figure. (f−h) HRTEM images taken at red boxes in c−e. In each HRTEM image, lattice distances along different lattice orientations are denoted. (Inset of f−h) A Fast Fourier-transformed pattern taken from each HRTEM image.

surfaces, Oh also exhibits a comparable capacity retention such that 94.1% of the initial capacity is retained after 400 cycles. The trend of the capacity retention among the samples becomes amplified at a higher temperature of 55 °C (Figure 6b) because the Mn dissolution becomes more severe at this temperature. At 55 °C with the same charging and discharging conditions as the room temperature tests, Oh^T and Oh retain 71.3 and 71.2% of the initial capacities (113.6 and 102.4 mAh

g^{-1}) after 400 cycles, whereas PL loses its capacity very rapidly as it shows 39.1 mAh g^{-1} only after 40 cycles. At 55 °C, both Oh^T and Oh also exhibit robust cycling performance in the extended cycle number, as they retain 64.3 and 63.8% of the original capacities after 850 cycles, respectively (Supporting Information, Figure S4).

It has been known that the surface orientation dependence on the Mn dissolution is related closely to the stability of SEI
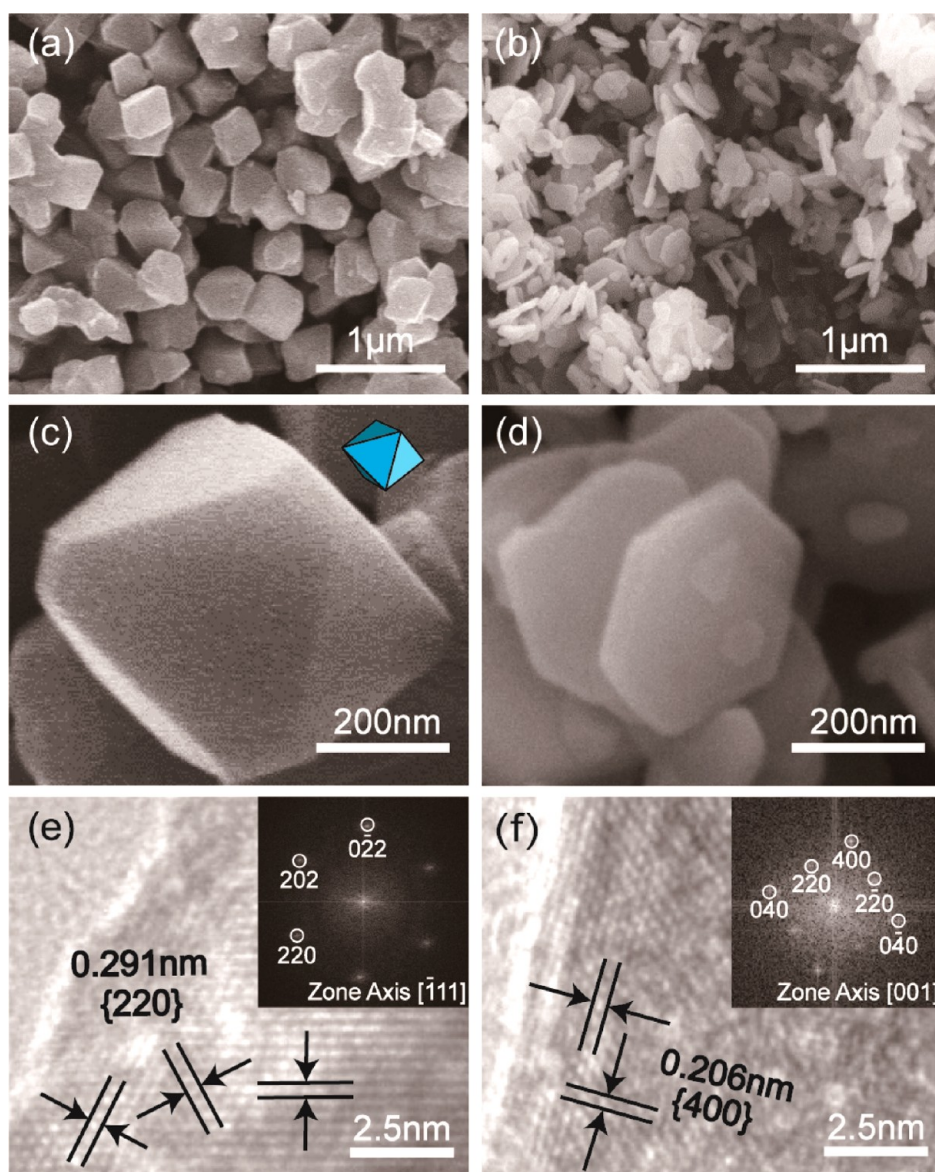
Figure 4. SEM and TEM characterizations of Oh and PL. Low-magnification SEM images of (a) Oh and (b) PL. (c−d) Same as (a−b) but at higher magnifications. (e−f) HRTEM images of (e) Oh and (f) PL. In each HRTEM image, lattice distances along different lattice orientations are denoted. (Inset of e−f) an FFT pattern taken from each HRTEM image.

layers and the atomic arrangement of Mn. In the SEI stability viewpoint, our previous investigation based on the thin films with controlled lattice orientations[17] indicates that the reconstructed (111) surface upon the exposure to the electrolyte forms stable SEI layers even in the early stage of electrochemical processes, which effectively mitigates Mn dissolution. The reactive surface characteristic was also reflected in the higher surface energy in a previous theoretical investigation.[33] In contrast, the (110) surface forms thicker SEI layers during cycling, representing less stable electrode−electrolyte interfacial behavior. On the other hand, in the perspective of the Mn atomic arrangement, Mn atoms are more densely packed at the (111) surface compared to the (110) and (100) surfaces. See Figure 6c−e for the atomic arrangements along the three surface orientations. It is anticipated that the less dense Mn arrangements along the (110) and (100) directions are more liable to interact with the electrolyte and thus accelerate the Mn dissolution. In addition, a recent

theoretical study[22,33] suggests that, unlike most other $LiMn_2O_4$ surfaces in which the Mn oxidation states are trivalent, a large portion of Mn ions at the (110) surface exist under the divalent state, making the surface more vulnerable to the Mn dissolution. In any case, for various reasons, the (111) surface is certainly more resistant against the Mn dissolution and plays a crucial role in our Oh^T structure for the improved cycle life. Electrochemical impedance spectroscopy (EIS) data in Supporting Information, Figure S5 also show consistent interfacial behaviors among the samples. While all of the three samples show the largest semicircle diameters prior to any electrochemical tests, PL exhibits a persistent increase in the diameter throughout cycling. By contrast, Oh^T and Oh show more stable behavior such that the diameters remain in narrower ranges of much smaller resistance values. Again, the rapid increase of the PL's interfacial resistance is ascribed to the more severe Mn dissolution that causes the SEI layers to continuously grow. Although a detailed mechanism for the
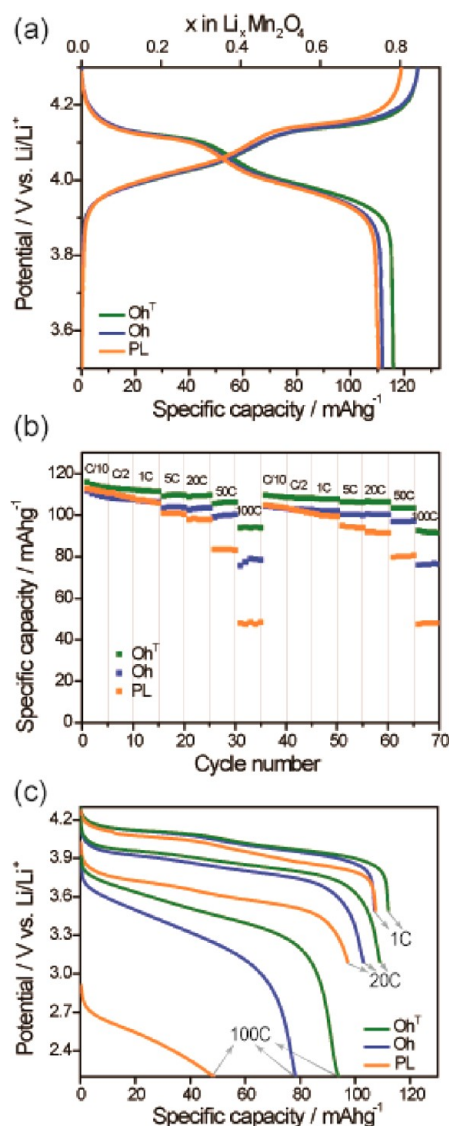
Figure 5. (a) Potential profiles measured at a 0.1 C-rate (14.8 mA g^{-1}) in the potential range of 3.5−4.3 V vs Li/Li$^+$. (b) Rate capability tests measured at various C-rates for discharge. See the Experimental Section for detailed test conditions. (c) Representative discharging profiles whose rate characteristics are shown in b.

decrease of interfacial resistance from the initial to subsequent cycles is nontrivial to grasp, it is speculated that, in the early stage of cycling, the reconstruction of SEI layers takes place to make the ionic diffusion more efficient. In addition, the small incomplete semicircle of Oh^T at the initial state (arrow in Supporting Information, Figure S5d), which is absent for Oh, is seemingly reflective of the truncated {110} surfaces that have been known[17] to have smaller interfacial resistances compared to those of the {111} surfaces.

The trend of the interfacial stability among the samples is also verified by SEM images at different stages (Figure S6). While the images taken after 10 cycles at 25 °C look similar to those of the as-synthesized for all of the three cases perhaps due to the relatively mild operating condition, the images taken after 850 cycles at 55 °C clearly show the consistent interfacial trend: negligible SEI formation for Oh^T and Oh, but markedly grown SEI layers for PL.

In conclusion, a series of results implicate that key electrochemical properties of LiMn$_2$O$_4$ are considerably dependent on its surface orientation. Our design concept of truncating a small portion of surfaces to support Li diffusion while leaving most remaining surfaces aligned along the crystalline orientations with minimal Mn dissolution enables excellent rate performance and cycle life simultaneously. The results suggest an ideal electrode structure of LiMn$_2$O$_4$, which is one of the most viable options for emerging large-scale battery cathodes.

Experimental Section. *Syntheses of Octahedral Mn$_3$O$_4$ with and without Truncated Surfaces.* A portion of 10 mmol of potassium permanganate (KMnO$_4$, Sigma-Aldrich, ACS reagent ≥99.0%) was first dissolved in 30 mL of deionized water. Then, 30 mL of polyethylene glycol (PEG, Samchun Chemical, M.W. ≈ 600) was added to the aqueous solution and briskly stirred for 20 min until a dark-brown suspension was made. The suspension was transferred into a 100 mL Teflon-lined stainless-steel autoclave, and hydrothermal reactions were carried out at 220 °C for truncated octahedron or 200 °C for bare octahedron for 8 h. After the reactions, using centrifugation, red-brown precipitants were collected and were then washed by the cosolvents of water and ethanol (9:1 in volume) several times. The particles were dried using a freeze-dryer to preserve the morphologies.

Synthesis of Mn(OH)$_2$ Nanoplatelets. A sample of 96 mmol of manganese chloride tetrahydrate (MnCl$_2$·4H$_2$O, Sigma-Aldrich, ACS reagent ≥98%) was dissolved in 1200 mL of deionized water, and the solution was slowly heated up to 85 °C.[34] A portion of 735 mL of 0.52 M ammonium hydroxide solution (NH$_4$OH, Sigma-Aldrich, ACS reagent 28.0−30.0% NH$_3$ basis) was added into the Mn solution. After 3 h of stirring, ivory-white precipitants were formed. The precipitants were washed several times by filtration using filter paper (Hyundai Micro No.53). Then, the precipitants were freeze-dried to preserve the morphologies.

Lithiation of Mn$_3$O$_4$ and Mn(OH)$_2$ To Complete LiMn$_2$O$_4$. The aforementioned Mn$_3$O$_4$ and Mn(OH)$_2$ were reacted with lithium hydroxide monohydrate (LiOH·H$_2$O, Aldrich, 99.95% trace metals basis) by solid state reactions. A stoichiometric ratio of 1.09:2 = Li/Mn was taken for the reactions. Both powders were mixed in absolute ethanol using mortar and pestle, and the mixture was then annealed at 650 °C for 10 h under air. The temperature ramp rate was 5 °C min^{-1}.

Characterization of Morphology and Crystal Structure. SEM (HITACHI, S-4800), TEM (JEOL, JEM-ARM200F), and XRD (RIGAKU, D/MAX-IIIC), respectively, were used to characterize the morphologies and microscopic and macroscopic crystal structures of LiMn$_2$O$_4$ with different structures.

Cell Preparation and Electrochemical Measurements. To prepare cathode electrodes, the synthesized LiMn$_2$O$_4$, denka black, and polyvinylidene fluoride (PVDF) were dissolved in *N*-methyl-2-pyrrolidinone in a weight ratio of 75:20:5. The well-mixed slurry was cast onto Al foil using the doctor blade technique. The electrode loading densities including all of the three components were 2.35, 2.57, and 2.37 mg cm^{-2} for Oh^T, Oh, and PL, respectively. To characterize the electrochemical properties, 2032 coin-type half-cells were used. In these cells, polyethylene separators (Toray Tonen Specialty Separator Korea Ltd.), 1 M lithium hexafluorophosphate (LiPF$_6$) dissolved in a mixture of ethylene carbonate (EC) and dimethyl carbonate (DMC) (EC/DMC = 1:1 = v/v, Soulbrain Co., Ltd.), and Li foil (Honjo Chemical Co.) were used as
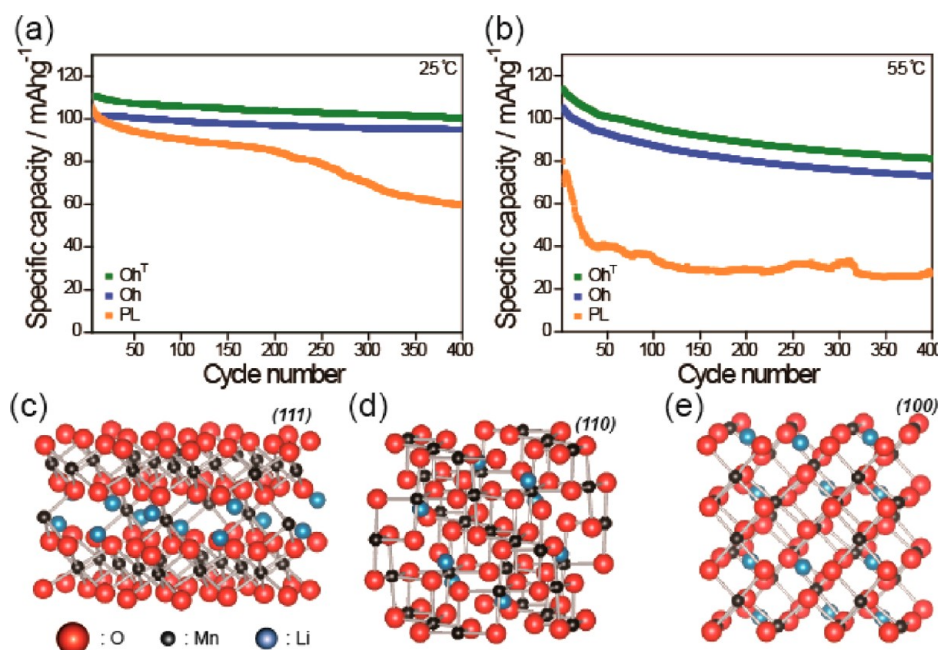
Figure 6. Characterization of cycle life and its dependence on the surface orientation. Discharge capacities over repeated cycles when cycled at 1C for charge and 10C for discharge at (a) 25 and (b) 55 °C. (c−e) Schematic illustrations of atomic arrangements along the different surface orientations: (c) (111), (d) (110), and (e) (100) orientations. Note that all of the three figures were drawn on the same scale for direct comparison of the atomic density.

separators, electrolyte, and counter/reference electrodes. The cell assembly processes were done in an argon-filled glovebox. The batteries were galvanostatically cycled (MACCOR series 4000) between 2.2 and 4.5 V vs Li/Li$^+$ at different current densities at 25 and 55 °C. For the rate capability tests, in the cases that C-rates for the discharge are below 1C, the C-rates for the charge and the discharge were the same. But, in the cases that C-rates for the discharge are equal to or greater than 1C, the C-rates for the charge were fixed to 1C. The EIS measurements were conducted (Bio-Logic VSP) using the same coin-cells in the frequency range of 10 mHz ∼ 1 MHz at the end of discharge at the designated cycles.

ASSOCIATED CONTENT

Ⓢ Supporting Information

SEM and TEM images of Mn_3O_4 and $Mn(OH)_2$, SEM images of $LiMn_2O_4$ platelet, cycling data in the extended cycle number, EIS data, and Ex-situ SEM images after cycles. This material is available free of charge via the Internet at http://pubs.acs.org.

AUTHOR INFORMATION

Corresponding Author

*E-mail address: kanno@echem.titech.ac.jp and jangwookchoi@kaist.ac.kr.

Notes

The authors declare no competing financial interest.

ACKNOWLEDGMENTS

REFERENCES

(1) Tarascon, J. M.; Guyomard, D. *Electrochim. Acta* **1993**, *38* (9), 1221−1231.
(2) Whittingham, M. S. *Chem. Rev.* **2004**, *104* (10), 4271−4302.
(3) Mizushima, K.; Jones, P. C.; Wiseman, P. J.; Goodenough, J. B. *Mater. Res. Bull.* **1980**, *15* (6), 783−789.
(4) Kang, B.; Ceder, G. *Nature* **2009**, *458* (7235), 190−193.
(5) Chung, S.-Y.; Bloking, J. T.; Chiang, Y.-M. *Nat. Mater.* **2002**, *1* (2), 123−128.
(6) Barpanda, P.; Ati, M.; Melot, B. C.; Rousse, G.; Chotard, J. N.; Doublet, M. L.; Sougrati, M. T.; Corr, S. A.; Jumas, J. C.; Tarascon, J. M. *Nat. Mater.* **2011**, *10* (10), 772−779.
(7) Recham, N.; Chotard, J. N.; Dupont, L.; Delacourt, C.; Walker, W.; Armand, M.; Tarascon, J. M. *Nat. Mater.* **2010**, *9* (1), 68−74.
(8) Tripathi, R.; Ramesh, T. N.; Ellis, B. L.; Nazar, L. F. *Angew. Chem., Int. Ed.* **2010**, *49* (46), 8738−8742.
(9) Sun, Y.-K.; Myung, S.-T.; Park, B.-C.; Prakash, J.; Belharouak, I.; Amine, K. *Nat. Mater.* **2009**, *8* (4), 320−324.
(10) Zhong, Q.; Bonakdarpour, A.; Zhang, M.; Gao, Y.; Dahn, J. R. *J. Electrochem. Soc.* **1997**, *144* (1), 205−213.
(11) Shin, Y.; Manthiram, A. *Electrochim. Acta* **2003**, *48* (24), 3583−3592.
(12) Shaju, K. M.; Bruce, P. G. *Chem. Mater.* **2008**, *20* (17), 5557−5562.
(13) Lee, H.-W.; Muralidharan, P.; Ruffo, R.; Mari, C. M.; Cui, Y.; Kim, D. K. *Nano Lett.* **2010**, *10* (10), 3852−3856.
(14) Hunter, J. C. *J. Solid State Chem.* **1981**, *39* (2), 142−147.
(15) Gummow, R. J.; de Kock, A.; Thackeray, M. M. *Solid State Ionics* **1994**, *69* (1), 59−67.
(16) Yamada, A.; Tanaka, M. *Mater. Res. Bull.* **1995**, *30* (6), 715−721.
(17) Hirayama, M.; Ido, H.; Kim, K.; Cho, W.; Tamura, K.; Mizuki, J. I.; Kanno, R. *J. Am. Chem. Soc.* **2010**, *132* (43), 15268−15276.
(18) Manthiram, A.; Vadivel Murugan, A.; Sarkar, A.; Muraliganth, T. *Energy Environ. Sci.* **2008**, *1* (6), 621−638.
(19) Arora, P.; White, R. E.; Doyle, M. *J. Electrochem. Soc.* **1998**, *145* (10), 3647−3667.
(20) Blyr, A.; Sigala, C.; Amatucci, G.; Guyomard, D.; Chabre, Y.; Tarascon, J. M. *J. Electrochem. Soc.* **1998**, *145* (1), 194−209.

(21) Hosono, E.; Kudo, T.; Honma, I.; Matsuda, H.; Zhou, H. *Nano Lett.* **2009**, *9* (3), 1045−1051.

(22) Benedek, R.; Thackeray, M. M.; Low, J.; Bučko, T. *J. Phys. Chem. C* **2012**, *116* (6), 4050−4059.

(23) Amatucci, G. G.; Blyr, A.; Sigala, C.; Alfonse, P.; Tarascon, J. M. *Solid State Ionics* **1997**, *104* (1−2), 13−25.

(24) Lim, S.; Cho, J. *Electrochem. Commun.* **2008**, *10* (10), 1478−1481.

(25) Lee, Y.-S.; Kumada, N.; Yoshio, M. *J. Power Sources* **2001**, *96* (2), 376−384.

(26) Yang, Y.; Xie, C.; Ruffo, R.; Peng, H.; Kim, D. K.; Cui, Y. *Nano Lett.* **2009**, *9* (12), 4109−4114.

(27) Chen, D.; Gao, L. *Chem. Phys. Lett.* **2005**, *405* (1−3), 159−164.

(28) Li, Y.; Tan, H.; Yang, X.-Y.; Goris, B.; Verbeeck, J.; Bals, S.; Colson, P.; Cloots, R.; Van Tendeloo, G.; Su, B.-L. *Small* **2011**, *7* (4), 475−483.

(29) Jiang, H.; Zhao, T.; Yan, C.; Ma, J.; Li, C. *Nanoscale* **2010**, *2* (10), 2195−2198.

(30) Wang, Z. L. *J. Phys. Chem. B* **2000**, *104* (6), 1153−1175.

(31) Huang, W.-C.; Lyu, L.-M.; Yang, Y.-C.; Huang, M. H. *J. Am. Chem. Soc.* **2011**, *134* (2), 1261−1267.

(32) Ohzuku, T.; Kitagawa, M.; Hirai, T. *J. Electrochem. Soc.* **1990**, *137* (3), 769−775.

(33) Benedek, R.; Thackeray, M. M. *Phys. Rev. B* **2011**, *83* (19), 195439.

(34) Lee, J.-M.; Kim, J.-S.; Hong, S.-K.; Lee, J.-J.; Ahn, H.; Cho, W. I.; Mho, S.-I. *J. Korean Electrochem. Soc.* **2012**, *15* (3), 172−180.